

Ubiquitous proximity to a critical state for collective neural activity in the CA1 region of freely moving mice

Yi-Ling Chen^{1,2}, Chun-Chung Chen^{1,3}, Yu-Ying Mei⁴, Ning Zhou⁵, Dongchuan Wu⁴, and Ting-Kuo Lee^{1,6,*}

¹Institute of Physics, Academia Sinica, Taipei, 11529, Taiwan

²Brain Institute, National Tsing Hua University, Hsinchu City, 300, Taiwan

³Institute of Neuroscience, National Yang Ming University, Taipei, 112, Taiwan

⁴Graduate Institute of Biomedical Science, China Medical University, Taichung, 404, Taiwan

⁵iHuman Institute, ShanghaiTech University, Shanghai, 201210, China

⁶Department of Physics, National Sun Yat-sen University, Kaohsiung, 804, Taiwan

*tklee@phys.sinica.edu.tw

ABSTRACT

Using miniscope recordings of calcium fluorescence signals in the CA1 region of the hippocampus of mice, we monitor the neural activity of hippocampal regions while the animals are freely moving in an open chamber. Using a data-driven statistical modeling approach, the statistical properties of the recorded data are mapped to spin-glass models with pairwise interactions. Considering the parameter space of the model, the observed system is generally near a critical state between two distinct phases. The close proximity to the criticality is found to be robust against different ways of sampling and segmentation of the measured data. By independently altering the coupling distribution and the network structure of the statistical model, the network structures are found to be vital to maintain the proximity to the critical state. We further find the observed assignment of the coupling strengths makes the net coupling at each site more balanced with slight variation, which likely helps the maintenance of the critical state. Network analysis on the connectivity obtained by thresholding the coupling strengths find the connectivity of the networks to be well described by a random network model. These results are consistent across different experiments, sampling and segmentation choices in our analysis.

Introduction

The CA1 region of hippocampus is an area of brain that is important for representing space information of the environment¹. Notably, place cells, the neurons that respond to a certain location or landmark in the environment, are first discovered in this region. Recently developed technologies such as miniscopes² allow optical recording of large numbers of neurons in this region while the animal is freely behaving in an experimental environment. Through calcium (Ca^{2+})-dependent fluorescence, the firing activities of neurons can be inferred simultaneously. This opens up the possibility for studying population coding in these regions of the brain.

To understand implications of the large volume of data, maximum-entropy modeling^{3,4} has been used to match the statistical properties of the observed firing images to that of a pairwise-interaction model of binary spin glass. While only matching the first and second order correlation statistics of the spins, such models have been shown to well reproduce the higher-order correlations as well as other properties of the observed data for the neural systems^{5,6}. Generalizing the model system to a broader parameter space, it has also been shown that the original parameter values corresponding to the observed brain images are poised near a critical point in the parameter space, consistent with the so-called critical brain hypothesis⁷⁻⁹.

To find the best values of model parameters that reproduce the statistical properties of observed data, we use the Boltzmann learning (BL) method¹⁰, which amounts to performing gradient descent on the Kullback–Leibler (KL) divergence¹¹ between the observed and modeled distributions of the binarized system states.

For many of the reported cases in statistical modeling of neural dynamics, in the proximity of a critical state seems to be a common observation for these systems. Here we refer the system to be in the proximity of a critical state simply because the true critical state should be considered for an infinitely large system while we only consider 60 to 100 neurons here. Even when the system size is finite, many properties are still quite similar to the critical state¹². Since the recorded neurons are only a very small fraction of the total neurons, it is desirable to verify whether the same conclusions would have been reached had the systems been sampled or segmented differently. Based on the miniscope data from four different experiments, the fitted models

corroborate the robustness of the proximity to a critical state under different subsampling and segmentation processes. The recovered best-fitted parameters of the external fields and the couplings in statistical modeling can reproduce the observed mean and pairwise correlations accurately. Similar distributions of these structural parameters are found under different sampling and segmentation conditions.

Having established the stability of the model parameters, we further analyze the connectivity of the inferred spin networks with different thresholds on the coupling strength and calculate their network properties, such as, cluster coefficient, average path length, and degree distribution. The network turned out to be well-described by a random network model¹³ for all experiments and subsamples when various thresholding criteria of connectivity are applied.

The main result is presented in section Results. The structure of the coupling strength parameters and the criticality of the systems are examined in section Parameters of spin-glass model. In section Analysis of network connectivity, the network connectivity is analyzed with different thresholds. It shows the property of a random network model. The discussion is in the section Discussion. The statistical modeling is described in section Methods.

1 Results

In order to compare the fitted parameters of local field h and coupling J for the four datasets, their distributions are calculated and shown in Fig. 1A and Fig. 1B, respectively. The detail is described in the Supplementary S1. The mean values and their standard deviations are listed in Table 1. Since neurons or the identified regions of interests (ROIs) in these systems in general favor silent states, the mean values of the local fields are all negative. The distributions of h are quite broad but mostly have values within the same range of -3 to 1 for the four cases. The mean values of J are all very small and it is close to the Gaussian distribution except the long tails at both ends. Actually, the long tail at the positive end is a bit more extended than the Gaussian. More detailed validation of the parameters is in Supplementary S2 and model predictions in the Supplementary S3.

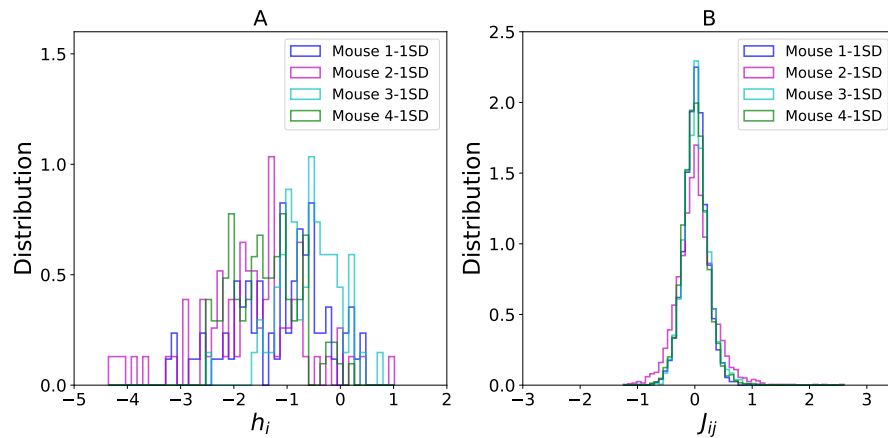


Figure 1. Distributions of best-fitted local field and coupling. **A.** The distributions of the best-fitted local field h in the four mice **B.** The distributions of the best-fitted coupling J .

Table 1. The means and standard deviations (in parenthesis) of the distributions shown in Fig. 1.

dataset	local field h	coupling J
Mouse 1-1SD	-1.12 (± 0.87)	0.01 (± 0.21)
Mouse 2-1SD	-1.68 (± 1.04)	0.01 (± 0.33)
Mouse 3-1SD	-0.60 (± 0.55)	0.02 (± 0.22)
Mouse 4-1SD	-1.41 (± 0.63)	0.01 (± 0.23)

1.1 Robustness of the critical behavior of the four datasets

To characterize the thermodynamic properties of the model, we extend the parameter space to include arbitrary T and calculate the specific heat of the model

$$C_v = \frac{1}{NT^2} \sigma^2(E)$$

where $\sigma^2(E)$ is the variance of energy, as a function of temperature. As commonly seen in earlier studies^{5,7}, the specific heat curve exhibits a single peak around the original system temperature $T = 1$ for all four datasets from the experiments (Fig. 2).

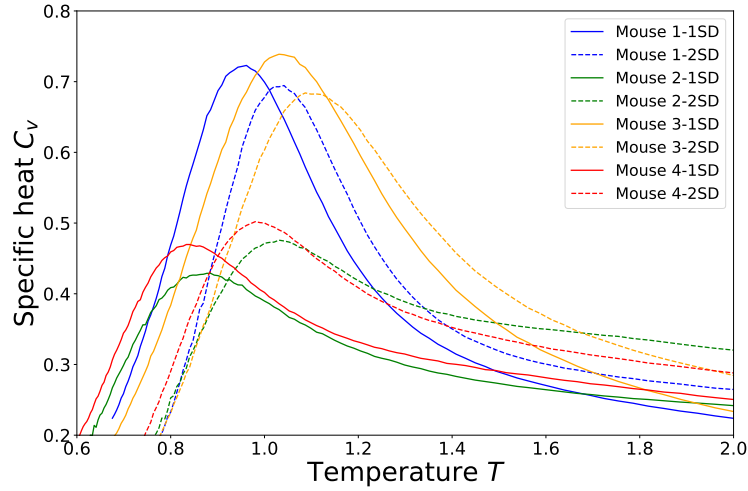


Figure 2. Specific-heat curves. Specific-heat curves for statistical models for the four experiments. The experimental data is at $T = 1.0$. The solid (dashed) curves are obtained with segmentation threshold of 1 and 2 standard deviation (SD) $\sigma(L_i^{\text{Ca}^{2+}})$ for the calcium-dependent fluorescence trace of each ROI i .

In the thermodynamic limit where the system has an infinite number of spins¹⁴, the specific-heat peak can diverge and signify a critical point of the system. However, as shown in Ref¹⁴, when there is only a finite number of spins, the specific heat will have a peak near the critical temperature. The peak becomes broader and peak temperature (T_p) moves away from the true critical temperature for systems with fewer and fewer spins. Our result shows T_p close to 1, where $T = 1$ is the temperature model parameters are determined from the dataset. This indicates that the observed system has a thermodynamic temperature near the critical point of our deduced spin-glass model. In other words, the observed neural state happens to be close to the boundary of two phases in the model spin system. It should be noticed that the thermodynamic temperature mentioned here is meaningful only in the model-parameter space and it is not related to the physical temperature of the real neural system. In our discussion below, we will identify the T_p of specific heat as the critical temperature.

To make sure that the observed critical state is not incidental to our choice of segmentation threshold, it is important to repeat the calculations using 2 times the standard deviation of each calcium trace as the binarization threshold. The resulting specific-heat curves using both $\sigma([Ca^{2+}]_i)$ (referred to as 1SD from now on) and $2\sigma([Ca^{2+}]_i)$ (2SD) as thresholds are shown in Fig. 2. The peak positions of specific heat as listed in Table 2 are all close to $T = 1$. In addition to the peak temperature of the specific heat, the critical point of the spin system can also be identified with the maximum of the slope dm/dT ¹⁵, where the magnetization m is thermodynamic average of the sum of all the spins. The detail about m vs T is discussed in the Supplementary S3 temperature dependence of the magnetization. To compare the critical temperatures obtained from both criteria, the temperatures of peak magnetization slope dm/dT are plotted against the temperatures of peak specific heat C_v for all calculated cases of various thresholds, subsamples, and mice in Fig. 3. The plot of magnetization slope dm/dT vs. temperature for Mouse 1-1SD is shown in the Supplementary Figure S7. This is the most important result of this work that we find these critical temperatures within 20% of $T = 1$ showing a ubiquitous proximity to a critical state as listed in Table 2 for all cases. The data in Fig. 3 also reveals an interesting correlation that the peak temperatures of both dm/dT and C_v are either greater or smaller than 1 together. It is well known for this kind of model¹² with a finite number of spins, the peaks of dm/dT and C_v will move away from the ideal critical temperature in the same way.

1.2 Robustness of the critical behavior of the random subsamples

While the volume of the acquired data in the experiments may be large, it typically represents only a very small portion of the neural systems. Or, the measurements may not have single-cell resolution. Additionally, the way of segmenting the recordings into discrete states may further discard a significant amount of the information from the measurements. With all these uncertainties, it requires us to further examine the conclusion of the last section that the data represents a state in the proximity of a critical state. One approach to address this issue is by studying subsamples consists of a subset of ROIs randomly selected from the original experimental set. Then, each is treated as a new set of data and the calculations are repeated to find

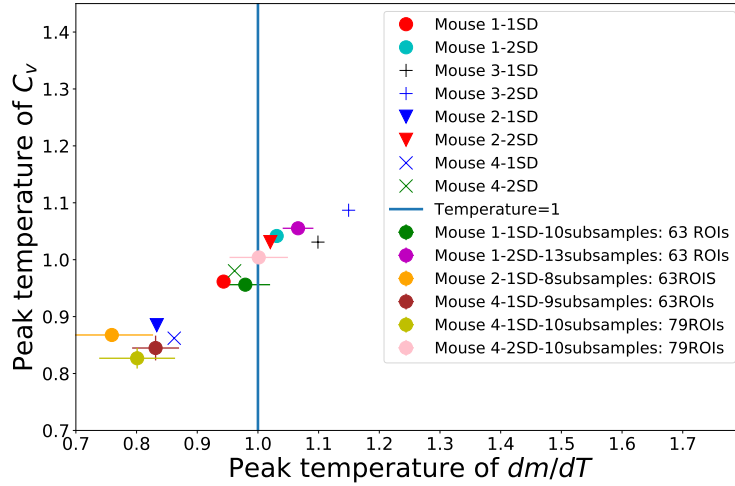


Figure 3. Peak temperature of dm/dT versus Peak temperature of C_v . Critical temperature determined by the peak of specific heat (vertical axis) versus that determined by the peak of magnetization slope (horizontal axis) for the four mice under different ways of segmentation and subsampling.

Table 2. Peak temperature of dm/dT versus peak temperature of C_v for four different experiments. Using different thresholds for segmentation, and some random subsamples of given size from the measured data. For multiple subsamples of the same size and from the same data, the mean values of the peak temperatures are shown followed by their standard deviations in parenthesis.

dataset	peak of dm/dT	peak of $C_v(T)$
Mouse 1-1SD	0.94	0.96
Mouse 1-1SD-10subsamples: 63 ROIs	0.98(± 0.04)	0.96(± 0.01)
Mouse 1-2SD	1.03	1.04
Mouse 1-2SD-13subsamples: 63 ROIs	1.06(± 0.03)	1.05(± 0.01)
Mouse 2-1SD	0.83	0.88
Mouse 2-1SD-8subsamples: 63 ROIs	0.76(± 0.07)	0.87(± 0.01)
Mouse 2-2SD	1.02	1.03
Mouse 3-1SD	1.10	1.03
Mouse 3-2SD	1.15	1.09
Mouse 4-1SD	0.81	0.84
Mouse 4-1SD-9subsamples: 63 ROIs	0.83(± 0.04)	0.84(± 0.02)
Mouse 4-1SD-10subsamples: 79 ROIs	0.8(± 0.06)	0.83(± 0.02)
Mouse 4-2SD	0.96	0.98
Mouse 4-2SD-10subsamples: 79 ROIs	1(± 0.05)	1(± 0.01)

the best fitted model. Here we consider random subsets of sizes $N_s = 64, 32, 16,$ and 8 . Each size of the subsamples is repeated 16 times to estimate the standard deviation for the specific heat and the peak position as shown in Fig. 4.

The resulting peak positions of the specific heat show a weak dependence on the system size within 10% down to $N_s = 8$. Similar with the result discussed by¹⁴ for a system of nearest neighbor Ising model, the peak becomes broader and peak temperature further shifts away as the number of spins is reduced. Here we only show the subsamples of one dataset, Mouse 1 with 1SD. Similar result from the Mouse 4 with 1 and 2 SD is shown in the Supplementary Figure S8.

1.3 Parameters of spin-glass model

The coupling parameters of the spin-glass model obtained from statistical modeling constitute an effective or functional network structure that can reproduce the observed state properties. One can expect that such network structure may bear some significance pertinent to the functional dynamics of the brain. However, before such possibility is pursued, we need also to make sure the structure is quite generic with little dependence on segmentation and sampling. For all of results reported above, the coupling strength J has much larger influence than the local field h on the statistical properties of the model as long as h is

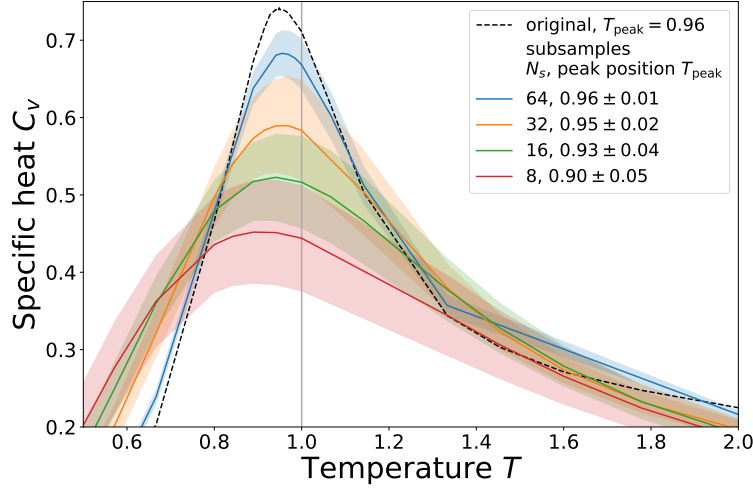


Figure 4. Specific heat curve of original Mouse 1-1SD and subsamples. Specific heat as a function of temperature for random subsamples of measured ROIs in Mouse 1-1SD experiment. The shaded regions represent the spread of the results for 16 samples for a given size of subsamples.

within the range shown in Fig. 1A. Hence, only coupling J will be considered in the analysis below.

1.3.1 Distribution and values of coupling strengths

To find out whether the distributions of coupling strength J obtained in Fig. 1B is sensitive to the number of neurons detected, subsets of neurons were randomly selected to form a number of subsamples. Then the model parameters of each subsample were calculated by the BL method. In Fig. 5, the coupling-strength distribution of the subsystems is compared to that from the full dataset and quantified using the Kolmogorov–Smirnov (KS) test (see the Supplementary S4 Kolmogorov–Smirnov test for the definition of KS statistic). Similar with the temperature dependence of specific heat, the KS statistic of subsamples shows weak size dependence and remains quite small until the subsample size reaches below 30 as shown in the inset of Fig. 5.

The robustness of the coupling strength distribution under the subsampling gives us an encouraging hope that, in our approach, it may not be necessary to measure all the neurons but only a relatively small subset of neurons to obtain a similar result.

Besides overall distribution, the value of the coupling strength between any two spins in a subsystem is compared to the coupling strength between the same spins in the original full system. Since, in principle, two very different datasets are separately fitted, the Pearson correlation coefficient between them should be very small. However, Fig. 6 shows the coefficients for the different subsamples all above 0.6. It is important to note that the subsystems have a very strong correlation with the original much larger system with Pearson coefficients between 0.75 to 0.9 for a system with only 40% neurons left. Details about calculations of Pearson correlation coefficients can be found in the Supplementary S4 Pearson correlation coefficients. Then, the next question is whether having a very similar pair-coupling structure is what allows the subsample systems to remain in the proximity of the critical state as shown in Figs. 3 and 4.

1.3.2 Importance of network structure

To answer the above question, it is important to first understand the unique characteristics of the pair-coupling structure. Thus two alterations to the coupling structure of the model are considered. Firstly, we reshape the coupling strength distribution into a Gaussian with the same mean and variance and randomly redraw the values of coupling strength while maintaining the rank of strength order for all spin pairs. The resulting specific heat-curves shown in Fig. 7 show a broad variation of peak temperatures. Unlike the original data shown in dashed line, most subsamples have the peak temperatures of specific heat far away from $T = 1$, which is the state related to the recorded data.

In the second case, the pair-coupling strength J_{ij} is randomly shuffled. This manipulation destroys the network structure while preserving the distribution of coupling strength. All the resulting specific-heat curves as shown in Fig. 8 have their peaks shifted to the right with the average value $\bar{T}_p \approx 2.05$. This implies that at $T = 1$, systems represented by the shuffled J are in the low temperature phase of their respective models. The two studies in this subsection reveal a couple of important characteristics of the pair-coupling structure. Randomly assigned coupling strength between pairs, in general, will not lead to a pair-interaction model with the peak of specific heat sitting near $T = 1$. The specific pair-coupling structure obtained from the experiment must be maintained to keep the state in the proximity of a critical state.

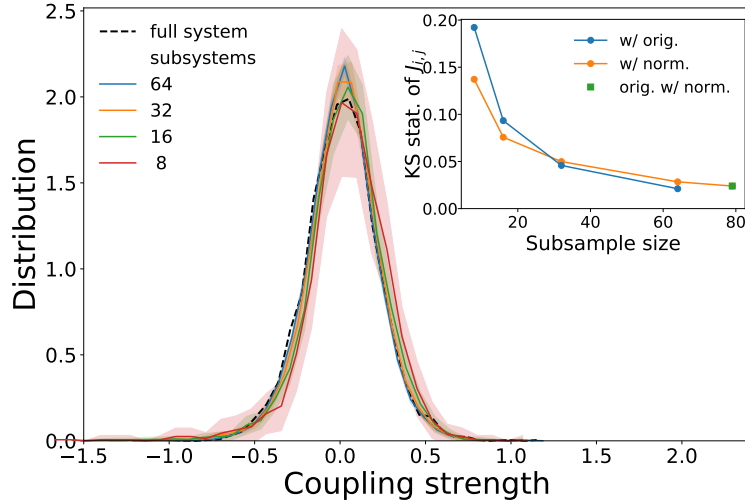


Figure 5. Distributions of coupling strength of original Mouse 1-1SD and subsamples. Distributions of coupling parameter J of the statistical models for the subsampled systems (drawn lines) compared with that for the original system (dashed line). The shaded area is the standard deviation estimated using 16 randomly drawn subsamples for each subsample size. The inset shows the Kolmogorov–Smirnov (KS) statistics of the subsamples with original (orig.) and a Gaussian (norm.) of the same mean and variance. The KS statistic between the distribution for the original 79 ROIs of the Mouse 1-1SD system and a Gaussian distribution of the same mean and variance is marked with a square.

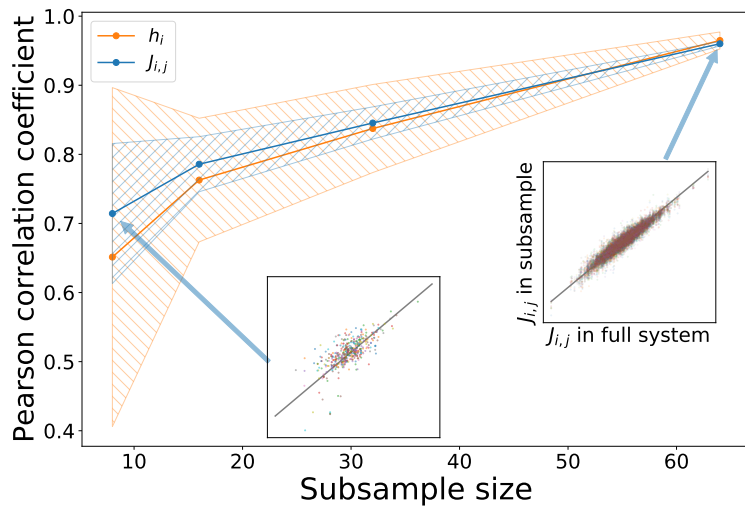


Figure 6. Pearson correlation coefficients of the best-fitted local field and coupling between the original Mouse 1-1SD and subsamples. Pearson correlation coefficients of the parameters J_{ij} and h_i between the models of subsamples and the model for the original system of Mouse 1-1SD. The coefficients remain above 0.6 down to subsample size 8. The insets show comparisons of J_{ij} values between the subsamples (vertical axis) and the original (horizontal axis).

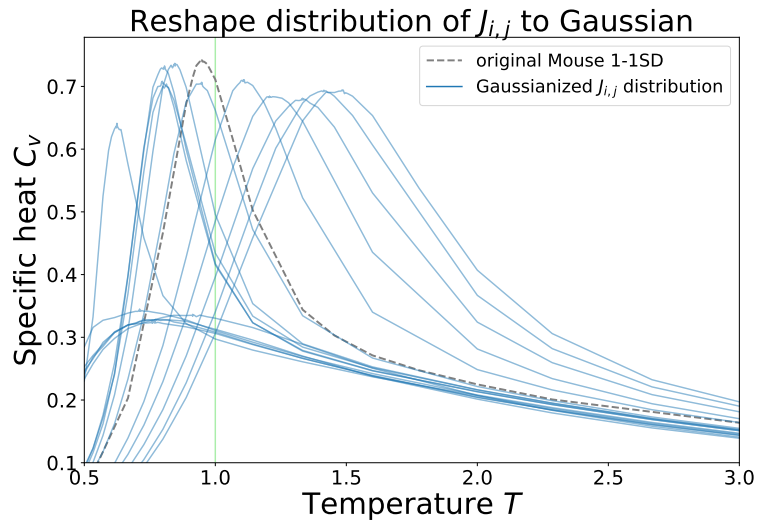


Figure 7. Specific-heat curves of the original Mouse 1-1SD and Gaussians. Specific-heat curves of models with new coupling strength values randomly drawn from a Gaussian distribution of the same mean and variance as the coupling distribution of the original model. The rank of coupling-strength order of the spin pairs are preserved when these new strength values are assigned.

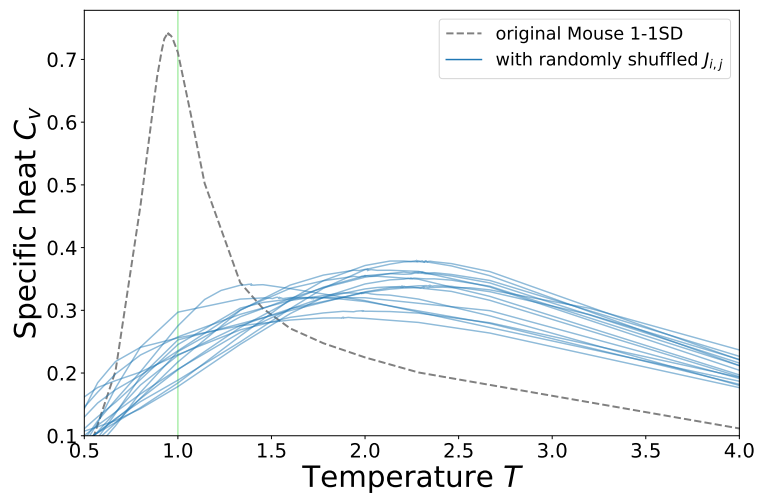


Figure 8. Specific-heat curves of original Mouse 1-1SD and shuffled network structures. Specific-heat curves of models with randomly shuffled network structures from the original statistical model of Mouse 1-1SD. The manipulation keeps the set of coupling strength values and reassigns them to different spin-pairs.

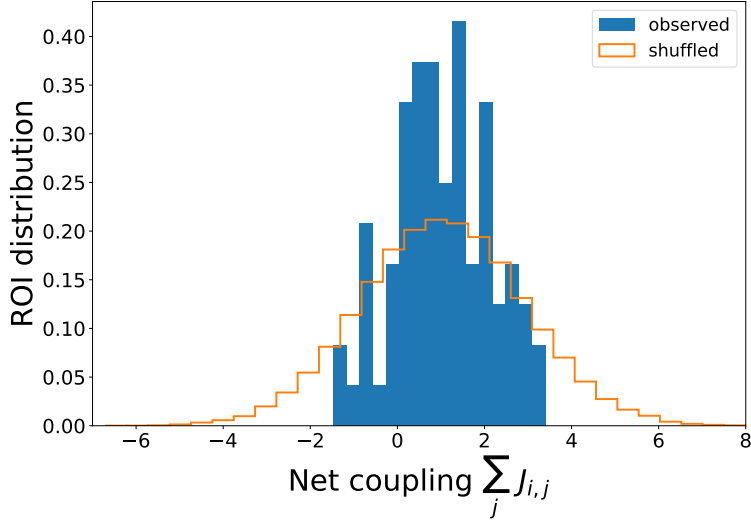


Figure 9. Distribution of net couplings for the ROIs of Mouse 1-1D. Distribution of net couplings $J_i^{\text{net}} \equiv \sum_j J_{i,j}$ for the ROIs in the model of Mouse 1-1SD dataset (shaded area), compared with the average of net ROI coupling distribution of shuffled networks from the same coupling $J_{i,j}$ distribution.

1.3.3 Balanced network in net coupling

Further investigation of the resulting network reveals that the observed network is generally more *balanced* compared to a randomly shuffled model. That is, if we define the net coupling of an ROI as the sum of the coupling strengths of all links connecting to this ROI, $J_i^{\text{net}} = \sum_j J_{i,j}$, the distribution of net couplings for the observed network is much narrower compared to a typical randomly shuffled samples as shown in Fig. 9.

The narrower distribution of net ROI coupling can be observed for all our four experiments. (See the Supplementary S4 Distributions of net coupling strength of ROIs.) To see how the balance of the coupling strength distribution affects the criticality of a network, we repeatedly apply selective random swapping of the link strengths of a shuffled network in order to make its net-ROI-coupling distribution narrower. We find the peak of its specific-heat curve does move towards $T = 1$ as net couplings become more uniform. However, this process alone is still insufficient to make the model as critical as what is observed experimentally. For the model of Mouse 1-1SD, the peak temperature of specific heat moves from 2.05 ± 0.28 to 1.65 ± 0.21 when randomly shuffled model is rebalanced to as good as the observation, and to 1.35 ± 0.25 at the limit of the balancing update when the net ROI coupling distribution is twice as narrow as the observation. Again, it is not easy to obtain a model with the peak temperature at $T = 1$.

1.4 Analysis of network connectivity

In the section discussed above, the network structure obtained from the mice data shows several very interesting characteristics that are important to the results presented so far. But what kind of network structure is it? Here we will try to answer this question. First, let us define some quantities that are commonly used in classifying network structure. For a connected network G consists of the set of vertices (nodes or ROIs) V , the average local clustering coefficients of the network is given by^{16,17}

$$\text{CC}(G) = \frac{1}{|V|} \sum_{v \in V} \text{CC}(v), \quad (1)$$

where the local clustering coefficient $\text{CC}(v)$ of a vertex v is defined as

$$\text{CC}(v) \equiv \frac{2N_v}{k_v(k_v - 1)}, \quad (2)$$

where k_v is the degree or the number of edges/bonds of v , and N_v is the number of connected vertex pairs whose both vertices are connected to v . The path length $d(v_1, v_2)$ is the minimal number of links that connect the vertices v_1 and v_2 to each other. The average path length $L(G)$ of a graph G is the average path lengths over all vertex pairs in the graph^{16,17}.

In the model, the coupling J_{ij} has both positive and negative values, hence it is separated into excitatory and inhibitory network with positive and negative J , respectively. To examine the structure more carefully, the properties of excitatory network

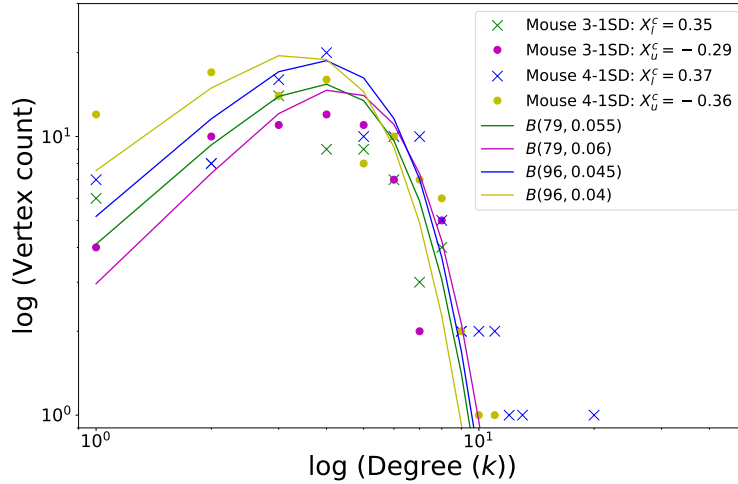


Figure 10. The log-log graph of degree distributions. The log-log plot of degree distributions at the critical threshold X_l^c in the excitatory networks and the critical threshold X_u^c in the inhibitory networks with their fitted binomial distributions.

will be calculated with a lower threshold X_l for J_{ij} , so that only bonds or edges with $J_{ij} > X_l$ will be considered. For larger X_l , there are few edges or bonds between nodes and few nodes are connected. But as X_l decreases, more connections are forming and all the nodes may become connected. Thus the degree distribution, clustering coefficient and path length will all depend on the lower threshold value X_l . There is a critical value X_l^c that for $X_l > X_l^c$, the network is disconnected such that not all the nodes are connected in one maximum cluster and we have isolated clusters or nodes. Similarly, properties of inhibitory network changes with the upper threshold X_u , when only bonds with coupling J_{ij} less than X_u are considered. There is also a critical threshold X_u^c that for $X_u < X_u^c$, the network is disconnected.

In a typical random graph model, the degrees follow a binomial distribution $B(k, p)$ ¹⁸, where k is the degree and p is the probability of having an edge. One of the earliest random graph models is the Erdős–Rényi model¹³, where the graphs is characterized by a parameter p for the probability of finding an edge between a given pair of vertices and there is no correlation between any edges. For networks of a large size N , a sharp transition occurs at the threshold $p = p_c = \log N/N$: The networks will almost surely be connected for $p > p_c$ and almost surely be disconnected for $p < p_c$ ¹³.

In Fig. 10, the degree distributions at the critical thresholds for all excitatory X_l^c and inhibitory X_u^c cases are plotted and compared with the corresponding binomial distribution.

The fraction of bonds between all possible pairs of vertices in the network is a function of X_l (X_u) for the excitatory (inhibitory) network and it is considered the same as probability p in the Erdős–Rényi model. At X_l^c and X_u^c , the fraction of bonds p_c is the probability p at the critical thresholds. As seen in Fig. 11, the values of p_c for all the excitatory and inhibitory cases of all our experiments are close to the predicted values $\log N/N$ ¹³ from the random network model. The deviation is probably due to the small size of our networks.

2 Discussion

While criticality have been observed in neural signals of many studies of brains, it is generally not very clear how universal these phenomena of critical states are. In the process of mapping the brain dynamic to simple statistical model, many details and much information is discarded. Furthermore, even with the ever improving technology in experimental studies of brains, the observed signals generally can only represent a small part of the entire system. In the current study, we verify the robustness of the proximity to a critical state in the CA1 recordings from four free-moving mice. We use different thresholds and different ways of subsampling the available ROIs into different sizes. The critical temperatures as determined by the peak of specific heat as well as the peak of magnetization slope are summarized in Fig. 3 for all considered cases of thresholding and subsampling of the data from the four mice. Majority of the peak temperature values are within 10% of $T = 1$ that is the temperature used to fit the experimental data. Thus the proximity to a critical state seems to be very robust against variations in measurement and analysis.

Along with the critical state, we also verify the structure of the coupling network of the statistical model is robust under random subsampling down to size 8. When comparing the distribution of the coupling strength of subsamples with the original model, we find the KS statistic remains small or comparable to the KS statistic between the original model and a Gaussian for

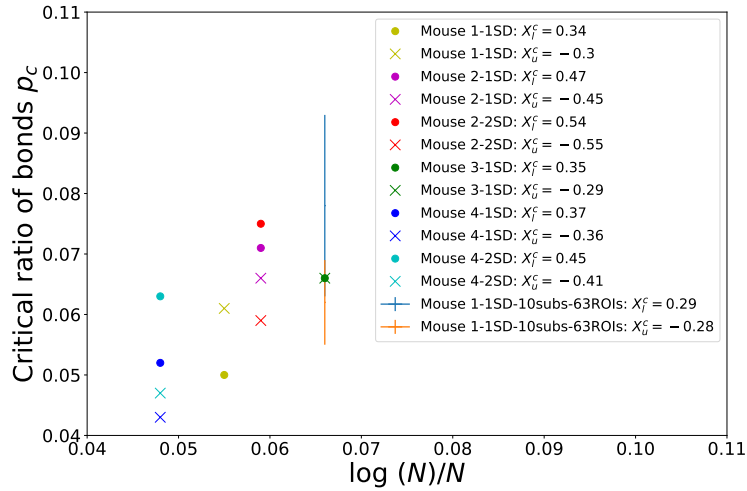


Figure 11. The prediction $\log(N)/N$ versus the critical fraction of bonds p_c . The critical fraction of bonds p_c when the networks start to break apart from one connected component versus the prediction $\log(N)/N$ from the random network model with N being the system size.

subsample sizes down to 30 (see Fig. 5). For subsample size smaller than 30, the KS statistic of a subsample increases quickly. This suggests that a minimal number of ROIs of 30 in experimental measurement may already have the main properties of the model represented. To understand the significance of the properties of the structure of the coupling network uncovered by the statistical modeling, the best-fit model is perturbed by independently changing the shape of the distribution and its network structure (see Figs. 7 and 8). While this proximity to a critical state seems to be very robust against variations in measurement, random shuffling of the bond coupling strength or assigning a value according to a Gaussian distribution will move the system far away from the critical state of the model.

We further find that the observed networks are generally more balanced than random shuffles of the same networks. While that can not fully account for the observed proximity to a critical state, making a shuffled network more balanced does help to bring it closer to a criticality. On the other hand, from the application of different thresholding criteria, the connectivity of the networks appears well described by the random network model. This suggests that the connectivity may not be specific at the level of average path length or degree distribution. Thus, the factors contributing to the ubiquity of the critical state may be more subtle than one would expect. A possible explanation is that the integration of sensory information through layers of neurons that precede the CA1 can effectively act as a renormalization process and filter out the irrelevant interactions or correlations leaving the most critical degrees of freedoms to be represented by the activities of the observed neurons at CA1.

Facing with the increasing volume of biological or social data, statistical modeling is currently the only quantitative and nontrivial approach that can be generally applied without any domain knowledge. Our results show that the application of statistical modeling to in vivo recording of brains can yield model properties that are robust to the arbitrariness and randomness of sampling and segmentation. Specifically, the network structure of the model is found to be crucial to the critical state. It would be interesting to find the basic principles required to construct such a network. It is also interesting to find biological conditions for the neurons to be at different critical states or non-critical at all.

3 Methods

3.1 Experimental setup and data processing

The male C57BL/6J mice (aged 8–12 weeks) were purchased from National Laboratory Animal Center Inc. (Taipei, Taiwan) and maintained under control conditions as follows: environmental temperature between 21–25 °C, a relative humidity 60 ± 10%, a 12:12-h light:dark cycle (light on from 08:00 to 20:00), and ad libitum access to food and water. All experimental procedures were performed according to China Medical University guidelines for the Care and Use of Experimental Animals and approved by the Institutional Animal Care and Use Committee of China Medical University.

To detect cytoplasmic free calcium activity in pyramidal regions of interest, 0.5 μL pENN. AAV. CamKII. GCaMP6f. WPRE. SV40 (Addgene, #100834, physical titer: $\geq 1.5 \times 10^{13}$ vg/mL) was injected into unilateral dorsal CA1 of the hippocampus (coordination: caudal from bregma -1.94 mm, lateral from bregma -1.25 mm, ventral from dura 1.35 mm) at 0.1 $\mu\text{L}/\text{min}$ for 7min in Zoletil-anesthetized mice. Two weeks after virus transduction, a Gradient-Index (GRIN) lens (1.8

mm diameter, 4.39 mm length, Edmund Optics Inc.) was implanted into dorsal CA1 (coordination: caudal from bregma -1.94 mm, lateral from bregma -1.25 mm, ventral from dura 1.6 mm). For the relief of pain and excessive innate immune responses to the GRIN lens implantation, anesthetized mice were given additional 10 mg/kg carprofen (Sigma-Aldrich), 0.2 mg/kg dexamethasone (Sigma-Aldrich) subcutaneously, and 10 mg/kg enrofloxacin (China Chemical & Pharmaceutical Co., Ltd.) intraperitoneally. After GRIN lens implantation, 0.4 mg/mL enrofloxacin were administered in the drinking water for 7–10 days to prevent bacterial infection. Related surgery information was obtained from the UCLA miniscope website (http://miniscope.org/index.php/Surgery_Protocol). After 3-week recovery period, we used the integrated miniature endoscope (miniscope V3) to check GCaMP+ regions of interest and then attached the baseplate to the skull of the lightly anesthetized mice with acrylic cement. After baseplate fixation, mice were ready to subsequent behavioral trainings.

The $30 \times 30 \times 30$ cm³ white square box surrounding with 2 distal visual cues on the contralateral walls was used to examine locomotor activity of awake-behaving mice. Behavior videos were recorded using Logitech C270 Webcam about 70 cm above the arena. After the 3-day habituation, the novel environment-induced hyperactivities were significantly decreased in mice. On the 4th consecutive day, behavior and calcium imaging videos were recorded simultaneously for 5–20 minutes in mice. All behavioral and dynamic calcium imaging data were analyzed by the UCLA Miniscope software based on the constrained nonnegative matrix factorization for microendoscopic data (CNMF-E) (the open-source MATLAB analysis package was obtained from https://github.com/daharoni/Miniscope_Analysis). The main data analyzed in the present study included mice positions, the intensity of calcium imaging data (the temporal traces C), and the deconvolution of calcium imaging data (calcium spikes).

In the current study, we consider the results from four separate experiments with four different mice. In experiment 1 (Mouse 1), 79 ROIs are identified from a 10 min recording. 72 ROI for 10 min. in experiment 2 (Mouse 2), 63 for 20 min. (Mouse 3) in experiment 3 and 96 for 10 min. (Mouse 4) in experiment 4.

For the statistical modeling in Methods, we convert the calcium signal trace $[Ca^{2+}]_i$ of each ROI, indexed by i , into binary states $s_i = \pm 1$ using the standard deviation (SD) of the trace as a threshold $\theta_i = \sigma([Ca^{2+}]_i)$,

$$s_i = \begin{cases} +1, & [Ca^{2+}]_i > \theta_i \\ -1, & \text{otherwise} \end{cases} \quad (3)$$

The collection of image frames of the CA1 recording becomes an ensemble of states for the system of $N = 79, 72, 63$ and 96 spins in the four experiments respectively. Details about transform experimental recordings to binary data can be found in the Supplementary S1 Transform experimental recordings to binary data .

3.2 Statistical modeling and multi-staged Boltzmann learning

3.2.1 All-to-all spin-glass model

To model the distribution of states for the experimental ensembles, we use an all-to-all pair-interaction spin-glass model similar to earlier works by, e.g., Schneidman et al., 2006³. The energy or Hamiltonian of the spin-glass model is given by

$$E(\mathbf{s}) = -\sum_i h_i s_i - \sum_{i < j} J_{ij} s_i s_j, \quad (4)$$

where spin at site i , $s_i = \pm 1$, h_i is the local magnetic field at site i , and J_{ij} is the coupling strength between two spins i and j . The second summation is over all $N(N-1)/2$ possible spin-pairs in the all-to-all system. The probability for the system to be observed at a given state $\mathbf{s} = \{s_i\}$ is given by the Boltzmann distribution

$$P(\mathbf{s}) = e^{-\beta E(\mathbf{s})} / Z, \quad (5)$$

where the normalization factor Z is the partition function

$$Z = \sum_{\mathbf{s}} e^{-\beta E(\mathbf{s})}, \quad (6)$$

and $\beta = T^{-1}$ gives the inverse temperature of the system. We set $T = \beta = 1$ for the fitting of experimental data.

The best-fitted values of parameters h_i and J_{ij} in the model (4) are obtained using a Boltzmann learning¹⁰ algorithm, which minimizes the KL divergence between the observed and model state distributions,

$$D_{\text{KL}} = \sum_{\mathbf{s}} P_{\text{data}}(\mathbf{s}) \ln \frac{P_{\text{data}}(\mathbf{s})}{P_{\text{model}}(\mathbf{s})}. \quad (7)$$

The gradients of the KL divergence in the h_i and J_{ij} parameter space are given by

$$\frac{\partial D_{\text{KL}}}{\partial h_i} = m_i^{\text{data}} - m_i^{\text{model}}, \quad (8)$$

$$\frac{\partial D_{\text{KL}}}{\partial J_{ij}} = C_{ij}^{\text{data}} - C_{ij}^{\text{model}}, \quad (9)$$

where $m_i \equiv \langle s_i \rangle$ is the magnetization of spin i and $C_{ij} \equiv \langle s_i s_j \rangle$ is the correlation between spins i and j . The angle brackets indicate averages over observed state configurations of the experiment system and over (Markov-Chain Monte Carlo, MCMC) simulation-generated configurations for the model system.

Various optimization methods based on gradient descent can be applied to find the minimum where the gradients (8) and (9) vanish, leading to $m_i^{\text{data}} = m_i^{\text{model}}$ and $C_{ij}^{\text{data}} = C_{ij}^{\text{model}}$. However for sizable systems, the convergence of the traditional Boltzmann learning can be slow or unstable with a fixed learning rate. Also for each step of the BL iteration, an extensive MCMC run can also be required for reaching desirable accuracies of the magnetization and correlation estimates of the model. We take a multi-staged Boltzmann learning approach in this paper that uses shorter MC runs for earlier BL iterations to save time at the cost of reduced accuracy and uses longer MC runs at the later stages of the BL to guarantee the precision of the convergence. Details are given in the the Supplementary S1 The multi-staged Boltzmann learning.

Acknowledgments

We are grateful for the funding support by the Ministry of Science and Technology of Taiwan (MOST) to TKL and CCC under the grant no. 108-2321-B-010-009-MY2, to YLC under grand no. 109-2123-M-001-001, and to DCW under grand no. 107-2320-B-039-061-MY3. Also, DCW is supported by the National Health Research Institutes under grant no. NHRI-EX110-10815NI and in part by the China Medical University Hospital under grant no. DMR-108-102.

Supplementary information

4 Supplementary Discussion S1: Statistical modelling and multi-staged Boltzmann learning

4.1 Transform experimental recordings to binary data

We analyze data extracted from a genetically-encoded calcium (Ca^{2+}) indicator, GCaNP6f and observe the dynamics of calcium in local CA1 regions of mice that are awake and freely moving in an open box. Unless otherwise mentioned below, we present details of our analysis on the Mouse 1 mouse data while similar results have also been obtained from the other three data sets. For our analysis, the calcium signal is first converted to binary data frames or states using the standard deviation of each ROI (neuron) as a threshold. Supplementary Fig. 12A shows the results for ROI 1, with the blue line representing the raw signal intensity of calcium imaging data at ROI 1 from a video of 17880 images frames (about 10 minutes with 30 frames per second). The green stars show the binary states $[-1, 1]$ scaled up by 100 intensity units representing the [active, silent] states, which are obtained by applying the threshold of $\sigma([\text{Ca}^{2+}]_1) \approx 63.2$ marked with the red line. Supplementary Fig. 12B shows the binary states s_i of all ROIs (neurons) for all data frames with black or white marking the active $s_i = +1$ or inactive $s_i = -1$ states when the intensity for an ROI i is respectively above or below its threshold $\theta_i = \sigma([\text{Ca}^{2+}]_i)$. We assign a vector of spin variables $\mathbf{s} = (s_1, \dots, s_N)$ with $s_i = 1$ for the i th active ROI and $s_i = -1$ for the i th silent ROI in 79 ROIs.

4.2 The multi-staged Boltzmann learning

In traditional Boltzmann learning (BL) algorithm, the model statistics m_i^{model} and C_{ij}^{model} in the gradients (Eqs. (8) and (9) in the main text) are calculated using Markov-chain Monte Carlo (MCMC) method with a fixed large number of steps to ensure their precision. An iteration in the BL includes the updates

$$h_i \leftarrow h_i + \eta (m_i^{\text{data}} - m_i^{\text{model}}) \quad (10)$$

$$J_{ij} \leftarrow J_{ij} + \eta (C_{ij}^{\text{data}} - C_{ij}^{\text{model}}) \quad (11)$$

of the parameters of the model, which is repeated until the model statistics match the data with desirable precision. To speed up this process, instead of using a fixed large number of steps in MCMC throughout all iterations of BL, we use a variable number of MCMC steps, adaptive on the size of the difference between the model and the data statistics. Specifically, we use the root-mean-square difference $d_{\text{rms}} \equiv C_{\text{rms}} + m_{\text{rms}}$, with

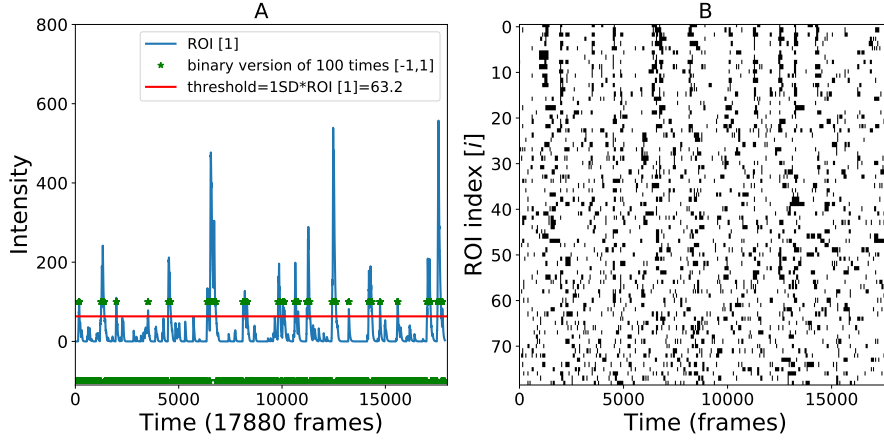


Figure 12. A. The calcium intensity of raw data of ROI[1] at 17880 time frames with the threshold= $1SD \cdot ROI[1]$ at 63.3 (red line) and its binary states (-1,1) times 100 as green points. B. The binary version of 79 ROIs use a threshold to each ROI $1SD \cdot ROI[i]$, $i = 0, 1, 2, \dots, 78$ in 17880 time frames (10 minutes).

Table 3. Variable number of MCMC steps in each BL iteration, adaptive to the RMS error in BL

d_{rms}	Number of MCMC steps T
$0.05 \leq d_{rms}$	10000
$0.009 \leq d_{rms} < 0.05$	100000
$0.005 \leq d_{rms} < 0.009$	1000000
$0.004 \leq d_{rms} < 0.005$	2000000
$0.003 \leq d_{rms} < 0.004$	3000000
$0.002 \leq d_{rms} < 0.003$	4000000
$d_{rms} < 0.002$	5000000

$$m_{rms} \equiv \sqrt{\frac{1}{N} \sum_i (m_i^{data} - m_i^{model})^2} \quad (12)$$

$$C_{rms} \equiv \sqrt{\frac{2}{N(N-1)} \sum_{i < j} (C_{ij}^{data} - C_{ij}^{model})^2} \quad (13)$$

to define the distance between the model and the data.

We start with $h_i = 0$ and $J_{ij} = 0$ as the initial condition of the BL. For each iteration, depending on d_{rms} , the MCMC runs for a variable number of steps T as listed in Supplementary Table 3 and the parameters h_i and J_{ij} are updated with rules of Eqs. (10) and (11) using $\eta = 0.01$ as the learning rate. After 100000 BL iterations, the set of h_i and J_{ij} that produced the minimum error d_{rms} is chosen as the best parameters of our model if this minimum d_{rms} is less or equal to 0.003. Otherwise, the set of h_i and J_{ij} is used as the initial condition for an extra BL run with learning rate $\eta = 0.003$ and a fixed number of MCMC steps $T = 7000000$ in each iteration until the error satisfies $d_{rms} < 0.003$.

The convergence of the model distribution to the data distribution is shown in Supplementary Fig. 13 for different learning algorithms. The hybrid BL in Supplementary Fig. 13 (blue line) converges faster than the traditional BL algorithm using the rate $\eta = 0.01$ and $T = 7000000$ (purple). In many cases of using traditional BL approach with 10000 MC steps, the result cannot converge in our running time (the red line in Supplementary Fig. 13). The main idea of the multi-staged BL algorithm is to correlate the learning rate with the desired accuracy represented by d_{rms} .

4.2.1 Model parameters

After the convergence of the multi-staged BL method, the best-fitted parameters of local field h and coupling J are first grouped into histograms. Then the histograms are normalized to have the total area of value 1 to become the distributions shown in Supplementary Figs. 14A and 14B for local field h and coupling J , respectively. The histograms have used the bin size

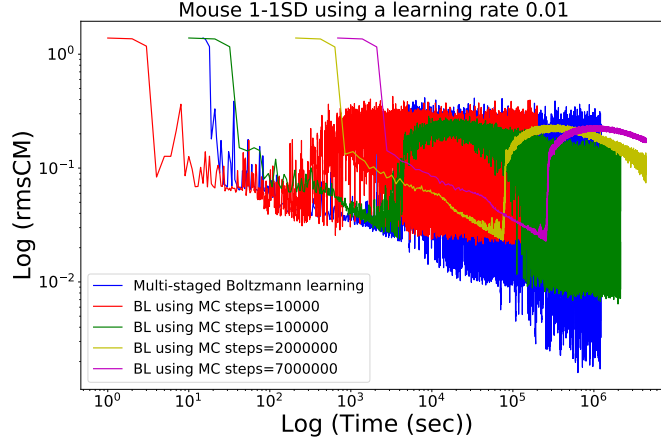


Figure 13. The log-log plot of the root mean-square difference versus the computer running time (sec) using multi-staged BL (blue color) and other traditional BL algorithm using different Monte Carlo (MC) steps. Traditional BL algorithms seem to be easier to get trapped in local minima. Our multi-staged MC method seems to be more efficient and also get consistent results for different runs.

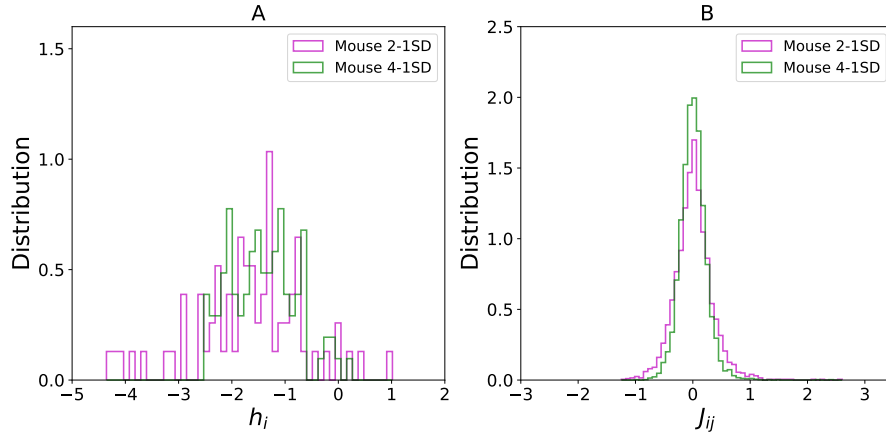


Figure 14. **A.** Distributions of the best-fitted local fields and **B.** couplings.

determined by

$$\frac{\text{maximum value of } h_i \text{ (and } J_{ij}) - \text{minimum value of } h_i \text{ (and } J_{ij})}{\text{number of bins}}, \quad (14)$$

where the number of bins is 50. The bin size of local fields is 0.11 and couplings is 0.08 in these cases.

5 Supplementary Discussion S2: Validation of the parameters

5.1 Matching the magnetization and covariance

We use the all-to-all spin-glass model and the multi-staged Boltzmann learning to get the best-fitted parameters by matching the observed mean (magnetizations) and pairwise correlation with calculated mean and pairwise correlation. The covariance is defined by

$$\text{Cov}_{(X,Y)} = \frac{\sum_i^N (X_i - \bar{X})(Y_i - \bar{Y})}{N} \quad (15)$$

,where \bar{X} and \bar{Y} are the means of X and Y , respectively. The correlation coefficient is $r = \frac{\text{Cov}_{(X,Y)}}{\sigma_X \sigma_Y}$, where $\text{Cov}_{(X,Y)}$ is the covariance matrix and σ_X and σ_Y are the standard deviations of X and Y , respectively. The comparison of observed with the calculated magnetizations M_i and covariance matrix Cov_{ij} are shown in Supplementary Figs. 15A and 15B, respectively.

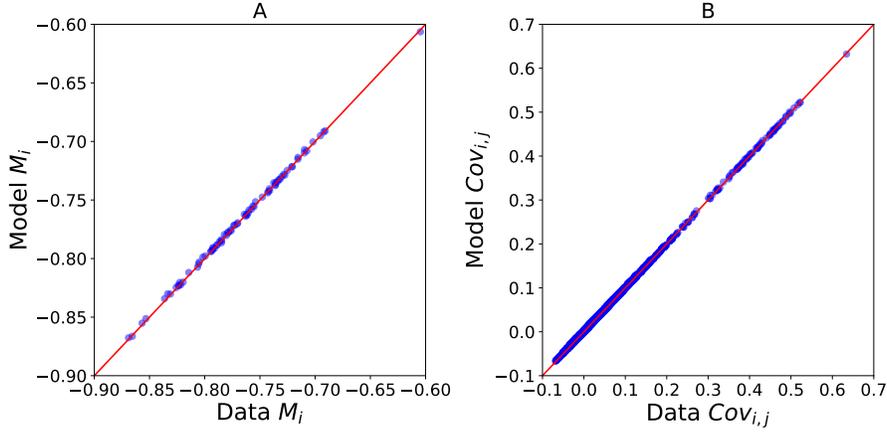


Figure 15. **A.** Matching the observed magnetizations with the calculated magnetizations. **B.** Matching the observed covariance matrix with the calculated covariance matrix using the data of Mouse 1-1SD.

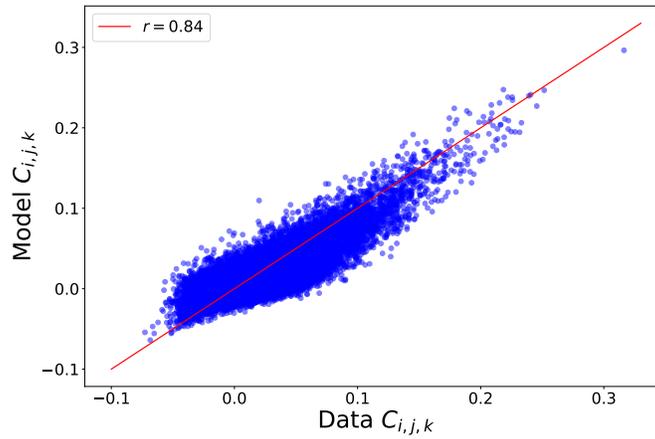


Figure 16. The observed versus calculated triple correlations using the data of Mouse 1-1SD.

5.2 Matching the high-order correlations

For a more detailed comparison of the collective behaviors in data with calculated populations, the triple correlation is calculated for a triplet of spins as given by

$$C_{ijk} = \langle (s_i - \langle s_i \rangle) (s_j - \langle s_j \rangle) (s_k - \langle s_k \rangle) \rangle. \quad (16)$$

The result of comparing the observed with calculated triple correlations in the case of Mouse 1-1SD is shown in Supplementary Fig. 16 with correlation coefficient $r = 0.84$. We included all possible triples of the observed data of 79 ROIs in 17880 frames and compared with calculated states of 79 ROIs in 17880 frames.

6 Supplementary Discussion S3: Model predictions

6.1 K simultaneously active neurons

The probability of having K out of N ROIs active simultaneously is shown in Supplementary Fig. 17 for the data Mouse 1-1SD. The agreement between model predictions and the data is reasonable good until $K=17$. Following Meshulam et al., 2017⁵, the uncertainty of the data is estimated by using random half of the data. With 100 samples the orange shade in Supplementary Fig. 17 represents the one SD.

The probability of K out of N ROIs active simultaneously is shown in Supplementary Fig. 17 for the data Mouse 1-1SD. Following Meshulam et al., 2017⁵, the uncertainty of the data is estimated by using random half of the data. With 100 samples the orange shade in Supplementary Fig. 17 represents the one SD. The probability of having all ROIs in silent or $s_i = -1$ state for the model is $P(0) = 0.021$ while the data has 0.015 ± 0.001 .

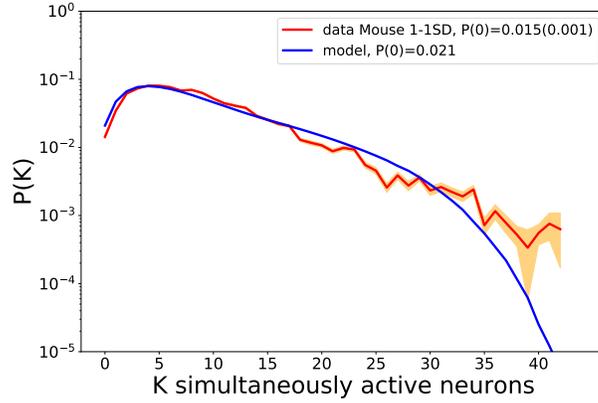


Figure 17. The probability of K out of 79 neurons in the population are active simultaneously of the model prediction (blue curve) and the mean of data prediction (red curve) and the error bars of 1SD using random halves of the data from 100 random trials (orange area).

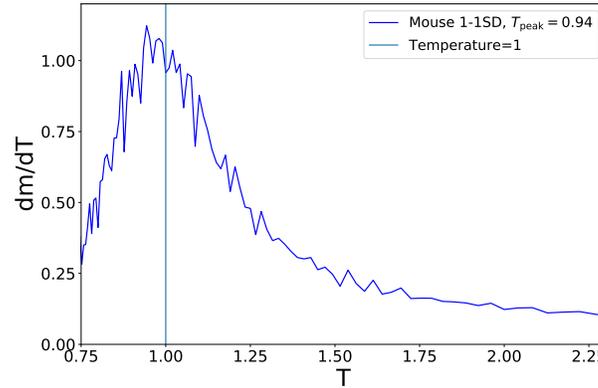


Figure 18. Magnetization slope dm/dT versus temperature in the case Mouse 1-1SD.

6.2 temperature dependence of the magnetization

The critical point of the spin glass system can be written as the maximum slope dm/dT (see, e.g., Huang, 1988¹⁵), where the magnetization m is the sum of all the spins, which is equal to the observed mean activity of 79 ROIs in the case of Mouse 1-1SD. Supplementary Fig. 18 shows the temperature dependence of magnetization slope dm/dT . The maximum peak value is situated at $T_p = 0.94$ which is very close to $T = 1$ as marked by the vertical line. Note that $T = 1$ is the temperature the experimental data is fitted for.

6.3 Temperature dependence of specific heat for subsamples

The peak temperatures of the specific heat for subsamples of Mouse 4 data was referred to in Supplementary Supplementary Fig. 3 of the main text. Here we show the detail temperature dependence of specific heat in Supplementary Supplementary Fig. 19. Nine and ten subsamples with 79 and 63 ROIs are randomly selected from the original data with 96 ROIs. Subsamples still show their proximity to the critical state. The other three datasets also have similar result.

7 Supplementary Discussion S4: Analysis of correlation of submaples with original data

7.1 Kolmogorov–Smirnov test

In Sec. V of the main text, the coupling distributions of the subsamples and original data were compared with the Kolmogorov–Smirnov (KS) test. Here we provide a little bit more information about the KS test and its statistic. But readers are referred to,

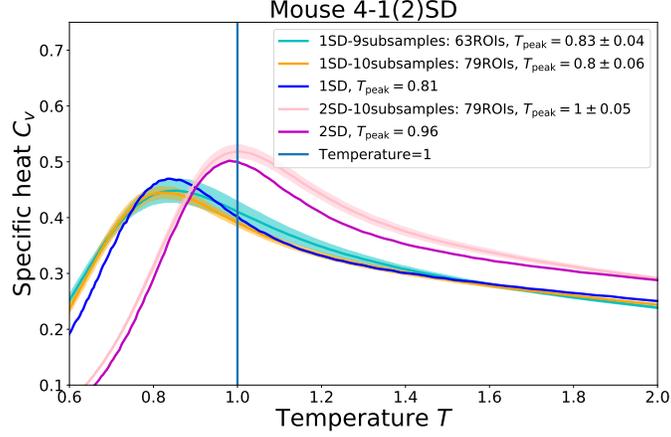


Figure 19. Specific heat curve from the statistical models for random subsamples of measured ROIs in Mouse 4-1(2)SD experiment. The shaded regions show the error bars of one standard deviation of uncertainty.

e.g., Sheskin, 2020¹⁹ for more details. The Kolmogorov–Smirnov statistic between two samples of variable x is defined as

$$D_{n,m} = \sup_x |F_{1,n}(x) - F_{2,m}(x)|, \quad (17)$$

where $F_{1,n}$ and $F_{2,m}$ are the cumulative distribution functions of the two samples of size n and m , respectively, and \sup is the supremum function. It quantifies the difference between the two distributions. When the measurements of each sample are drawn independently from an underlying probability distribution, the KS statistic can be related to the probability that the two samples are drawn from the same distribution. In the current study, we are using the KS statistic merely as a measure of how close two distributions are to each other.

7.2 Pearson correlation coefficients

Pearson correlation coefficients between subsamples and original sample are presented in Fig. 6 of the main text. Here we provide a little more detail of the calculations. Consider a subsample $\{s'_\alpha\}$, $\alpha = 0, \dots, N_S - 1$ of an original data set $\{s_i\}$, $i = 0, \dots, N - 1$ with the mapping $s'_\alpha = s_{i_\alpha}$ and the condition $i_\alpha \neq i_\beta$ if $\alpha \neq \beta$. The coupling strengths $J'_{\alpha\beta}$ of the statistical model for the subsample are obtained through fitting the mean and covariance of the size- N_S spin-glass system to the statistics of the subset of ROIs using the BL method. Since some spins of the original system are not included, the coupling strength between two subsample spins α and β is generally different from the coupling between the spins i_α and i_β in the model of the original size- N system. To find how they are related, we calculate the Pearson correlation coefficient between $J'_{\alpha\beta}$ and $J_{i_\alpha i_\beta}$ over all pairs α, β of the subsamples¹⁹,

$$\rho = \frac{\sum_{\langle \alpha, \beta \rangle} (J'_{\alpha\beta} - \bar{J}') (J_{i_\alpha i_\beta} - \bar{J})}{\sqrt{\sum_{\langle \alpha, \beta \rangle} (J'_{\alpha\beta} - \bar{J}')^2} \sqrt{\sum_{\langle \alpha, \beta \rangle} (J_{i_\alpha i_\beta} - \bar{J})^2}}$$

where $\bar{J}' \equiv 2 \sum_{\langle \alpha, \beta \rangle} J'_{\alpha\beta} / N_S (N_S - 1)$, and $\bar{J} \equiv 2 \sum_{\langle \alpha, \beta \rangle} J_{i_\alpha i_\beta} / N_S (N_S - 1)$ are the mean coupling strength of subsample bonds in the subsample and in the original system. For each subsample size N_S , the calculation is repeated for 64 random subsamples and the mean and variance of the Pearson correlation coefficients of their coupling strengths with the original system are used to plot the line and the shaded area in Fig. 6 of the main paper. The same calculations are also performed for the local field h_i with results shown in Fig. 6 as well.

7.3 Distributions of net coupling strength of ROIs

The net coupling strength of ROIs in Mouse 1 data set was shown in Fig. 9 of the main text. Below we include the results for the other three datasets in Supplementary Fig. 20.

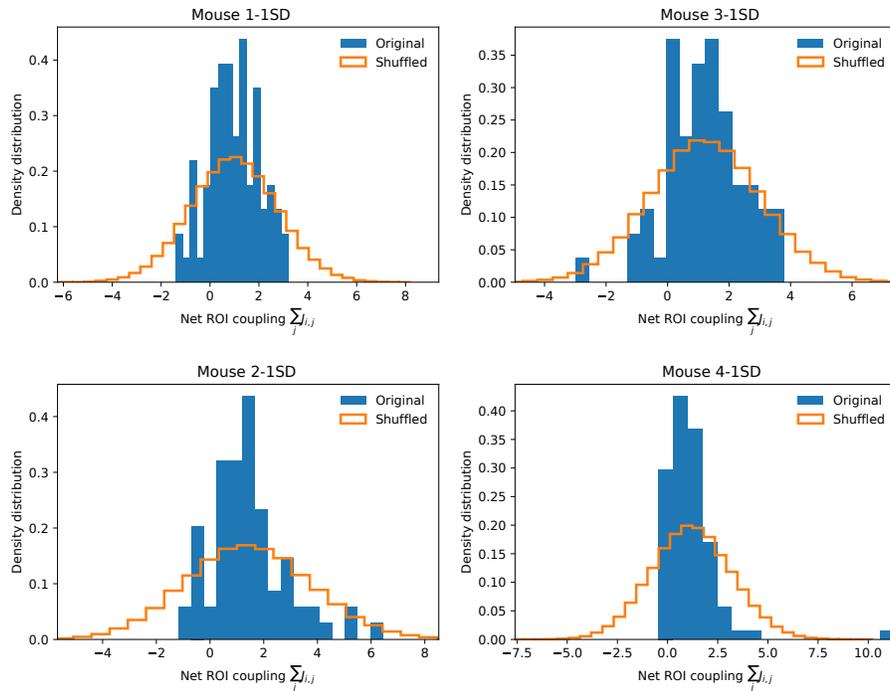


Figure 20. Net-ROI-coupling-strength distributions of the statistical model for all the four datasets

Author contributions statement

YYM, NZ and DW carried out the mouse experiment and wrote Methods: Experimental setup and data processing. YLC, CCC and TKL wrote the other part of the manuscript. All authors reviewed the manuscript. TKL conceived the idea and guided the project. YLC, and CCC performed the computations and all the figures in the main text and supplementary information.

Competing interests

The authors declare no competing interests.

References

1. O’Keefe, J. Place units in the hippocampus of the freely moving rat. *Exp. Neurol.* **51**, 78–109, DOI: [10.1016/0014-4886\(76\)90055-8](https://doi.org/10.1016/0014-4886(76)90055-8) (1976).
2. Ghosh, K. K. *et al.* Miniaturized integration of a fluorescence microscope. *Nat. Methods* **8**, 871–878, DOI: [10.1038/nmeth.1694](https://doi.org/10.1038/nmeth.1694) (2011).
3. Schneidman, E., Berry, M. J., Segev, R. & Bialek, W. Weak pairwise correlations imply strongly correlated network states in a neural population. *Nature* **440**, 1007–1012, DOI: [10.1038/nature04701](https://doi.org/10.1038/nature04701) (2006).
4. Tkacik, G., Schneidman, E., Berry II, M. J. & Bialek, W. Ising models for networks of real neurons. *arXiv:q-bio/0611072* (2006). ArXiv: q-bio/0611072.
5. Meshulam, L., Gauthier, J. L., Brody, C. D., Tank, D. W. & Bialek, W. Collective Behavior of Place and Non-place Neurons in the Hippocampal Network. *Neuron* **96**, 1178–1191.e4, DOI: [10.1016/j.neuron.2017.10.027](https://doi.org/10.1016/j.neuron.2017.10.027) (2017).
6. Tkačik, G. *et al.* Thermodynamics and signatures of criticality in a network of neurons. *Proc. Natl. Acad. Sci.* **112**, 11508–11513, DOI: [10.1073/pnas.1514188112](https://doi.org/10.1073/pnas.1514188112) (2015).
7. Mora, T. & Bialek, W. Are Biological Systems Poised at Criticality? *J. Stat. Phys.* **144**, 268–302, DOI: [10.1007/s10955-011-0229-4](https://doi.org/10.1007/s10955-011-0229-4) (2011).
8. Usher, M., Stemmler, M. & Olami, Z. Dynamic Pattern Formation Leads to $\frac{1}{f}$ Noise in Neural Populations. *Phys. Rev. Lett.* **74**, 326–329, DOI: [10.1103/PhysRevLett.74.326](https://doi.org/10.1103/PhysRevLett.74.326) (1995).

9. Beggs, J. M. The criticality hypothesis: how local cortical networks might optimize information processing. *Philos. Transactions Royal Soc. A: Math. Phys. Eng. Sci.* **366**, 329–343, DOI: [10.1098/rsta.2007.2092](https://doi.org/10.1098/rsta.2007.2092) (2008).
10. Ackley, D. H., Hinton, G. E. & Sejnowski, T. J. A Learning Algorithm for Boltzmann Machines. *Cogn. Sci.* **9**, 147–169, DOI: [10.1207/s15516709cog0901_7](https://doi.org/10.1207/s15516709cog0901_7) (1985).
11. Kullback, S. & Leibler, R. A. On Information and Sufficiency. *Annals Math. Stat.* **22**, 79–86, DOI: [10.1214/aoms/1177729694](https://doi.org/10.1214/aoms/1177729694) (1951).
12. Stanley, H. E. *Introduction to Phase Transitions and Critical Phenomena* (Oxford University Press, 1987).
13. Erdős, P. & Rényi, A. On random graphs I. *Publ. Math. Debrecen* **6**, 290–297 (1959).
14. Landau, D. P. Finite-size behavior of the simple-cubic Ising lattice. *Phys. Rev. B* **14**, 255–262, DOI: [10.1103/PhysRevB.14.255](https://doi.org/10.1103/PhysRevB.14.255) (1976).
15. Huang, K. *Statistical Mechanics* (John Wiley and Sons (WIE), 1988), 2nd edn.
16. Wang, X. & Chen, G. Complex networks: Small-world, scale-free and beyond. *Circuits Syst. Mag. IEEE* **3**, 6 – 20, DOI: [10.1109/MCAS.2003.1228503](https://doi.org/10.1109/MCAS.2003.1228503) (2003).
17. Chen, Q. & Shi, D. The modeling of scale-free networks. *Phys. A: Stat. Mech. its Appl.* **335**, 240 – 248, DOI: <https://doi.org/10.1016/j.physa.2003.12.014> (2004).
18. Feller, W. *An Introduction to Probability Theory and Its Applications, Vol. 1* (John Wiley and Sons, Inc., 1968), 3rd edn.
19. Sheskin, D. J. *Handbook of Parametric and Nonparametric Statistical Procedures, Fifth Edition* (CRC Press, 2020).